

# Bulk synthesis of silver-head colloidal rodlike micromotors

Yongxiang Gao,<sup>a\*</sup> Roel P.A. Dullens<sup>b</sup> and Dirk G.A.L. Aarts<sup>b</sup>

Received 00th January 20xx,  
Accepted 00th January 20xx

DOI: 10.1039/x0xx00000x

www.rsc.org/

Colloidal particles with asymmetric catalytic activities are emerging micro/nanomotors that harvest chemical energy for propulsion in fluids. It is of general interest to produce such particles with high performance, in large quantity and at low cost. In this paper, we present a facile bulk method to synthesize silver-head colloidal silica rods. These particles self-propel towards their active sites by reacting with hydrogen peroxide, and the velocity is tuned via the fuel concentration. We show that these motors are highly efficient: compared to the currently available chemical-phoretic micro/nanomotors they show similar performance of self-propulsion at fuel concentrations that are two orders of magnitude smaller.

## 1. Introduction

Biological motors fulfil intricate tasks robustly at the nano and microscale by consuming chemical energy to run against random Brownian motion. Emerging synthetic analogues are chemically-powered colloidal particles or micro/nanomotors<sup>1</sup>, which have attracted an increasing amount of attention due to their potential for applications, e.g. as cargo delivery systems<sup>2, 3</sup>, and for environmental remediation<sup>4</sup>, and also to understand fundamental aspects of active matter<sup>5-7</sup>.

At the colloidal scale, the Reynolds number is low, so viscous drag dwarfs inertia. In this regime, reciprocating moves that generate motion at high Reynolds number are no longer effective. Instead, symmetry breaking is the key for generating self-propulsion<sup>8</sup>. Janus colloidal particles with site-dependent chemical activities form a natural choice<sup>9, 10</sup> and as the chemical reactions are triggered asymmetrically, the particles are able to harvest and transduce the resulting energy into autonomous motion.

A canonical example of micro/nanomotors are platinum (Pt)-based colloidal Janus particles<sup>11-16</sup>, which are usually created by membrane-template assisted electrodeposition<sup>11</sup> or physical vapour deposition<sup>12</sup>. Through decomposition of hydrogen peroxide (H<sub>2</sub>O<sub>2</sub>), these motors have demonstrated a variety of mechanisms for self-propulsion, including self-electrophoresis<sup>11</sup>, self-diffusiophoresis<sup>17</sup> and bubble release<sup>16</sup>. Self-electrophoresis was proposed to account for the self-propulsion of bimetallic Au-Pt nanorods<sup>11, 18</sup>. The decomposition of H<sub>2</sub>O<sub>2</sub> is achieved through two half redox reactions that occur at the two ends of the particles, respectively. Specifically, electrons were produced at the Pt end and consumed at the Au end,

which results in an electric field. Meanwhile, protons are produced at the Pt end and consumed at the Au end. The ensuing migration of protons drags the fluid with them, causing a slip velocity between the particles and the surrounding fluid. On the other hand, self-diffusiophoresis relies on the generation of a concentration gradient of reaction products, which can be classified into neutral<sup>12</sup> and electrolyte-based ones<sup>19</sup>, depending on whether the solute carries charges. In the first case, the transportation of colloidal particles is driven by the pressure gradient given rise by the concentration gradient of neutral solutes<sup>19</sup>. In the second case, charged particles are driven to move by an electric field set up by asymmetric distribution of anions and cations that have different diffusivities<sup>19</sup>. Finally, in the case of self-propulsion via bubble release, oxygen (O<sub>2</sub>) produced from the decomposition of H<sub>2</sub>O<sub>2</sub> forms bubbles that grow as more oxygen is accumulated, which are then released from the particle as they are beyond a critical size<sup>16</sup>. The detachment results in a momentum change which propel the particle from its catalyst site. It is of general interest to produce micro/nanomotors of improved performance at high yield with less expensive materials, which has been the incentive for the continuous development of new fabrication techniques<sup>20</sup>.

Here, we present a simple wet-chemistry method that can produce micromotors in bulk quantities. The method combines the formation of Pickering emulsions, stabilized by chemically active silver nanoparticles, with the directional growth of silica rod-like particles<sup>21</sup>. This results in micro-rods composed of a hollow silver-enriched head and a silica tail. Note that the mechanism of our method is different from those for synthesizing MnO<sub>2</sub>-silica<sup>22</sup> and Fe<sub>3</sub>O<sub>4</sub>-silica Janus rods<sup>23, 24</sup> that were reported recently. It yields Janus rods with a different morphology and a significantly larger diameter. In the MnO<sub>2</sub>-silica and Fe<sub>3</sub>O<sub>4</sub>-silica studies, the emulsions were primarily stabilized by sodium citrate and Poly(vinyl pyrrolidone)<sup>21</sup>, with the size of the synthesized particles barely changed upon addition of nanoparticles. The activity between the silver head of our particles and hydrogen peroxide<sup>25-28</sup> and the difference in the diffusivity of the resulting ions is exploited here for self-propulsion based on an electrolyte self-diffusiophoresis mechanism<sup>19</sup>. The dynamics of the system at various fuel

<sup>a</sup> Institute for Advanced Study, Shenzhen University, Nanhai Avenue 3688, Nanshan District, Shenzhen, 518060, China. E-mail: yongxiang.gao@szu.edu.cn

<sup>b</sup> Department of Chemistry, Physical and Theoretical Chemistry Laboratory, University of Oxford, South Parks Road, Oxford OX1 3QZ, United Kingdom

† Footnotes relating to the title and/or authors should appear here.

Electronic Supplementary Information (ESI) available: [Schematics on electrolyte self-diffusiophoresis and Movie showing particle tracking at fuel concentration of 0 and 0.1 w%]. See DOI: 10.1039/x0xx00000x

concentrations are quantitatively characterized using image analysis routines. Furthermore, the self-propelled velocity and the corresponding Peclet number are evaluated and compared to those of the popular Pt-based colloidal motors in order to assess their performance.

The paper is organized as follows. We start by describing the experimental details in Section 2, including Materials, Silver nano-particle synthesis, Janus rod synthesis, Characterization, and Video microscopy. We then present the results and discussion in Section 3. In the end, we summarize our conclusions in Section 4.

## 2. Experimental

### Materials

Silver nitrate ( $\text{AgNO}_3$ ), Poly(vinyl pyrrolidone) (PVP,  $M_w=40,000 \text{ g mol}^{-1}$ ), 1-pentanol, absolute ethanol and Hydrogen Peroxide ( $\text{H}_2\text{O}_2$ ) were obtained from Sigma Aldrich, sodium citrate from Fisher Scientific, ammonia solution (25w%) from Merck Chemicals, and tetraethyl orthosilicate (TEOS, 98%) from Acros Organics. Deionized (DI) water (Millipore,  $18.2 \text{ m}\Omega$ ) was used throughout the work. All chemicals were used without further purification.

### Silver nano-particle synthesis

Silver nano-particles (AgNP)s were synthesized by reducing silver nitrate to silver with the  $-\text{OH}$  end group of PVP<sup>29</sup>. Typically, 6 g of PVP was dissolved in 8 ml of water by sonication (VWR ultrasonic cleaner) in a 20 ml vial. Then, 3 ml of 0.6 M aqueous solution of silver nitrate was added dropwise to the solution under magnetic stirring. The sample was left undisturbed at  $60^\circ\text{C}$  for 20 hours to react. After the reaction was finished, the solution was centrifuged at 12000 rpm (Eppendorf minispin) for 70 minutes and the supernatant was disregarded. The sediment was washed in water for 3 times before it was suspended in water.

### Janus rod synthesis

First, 1 g of PVP was dissolved in 10 ml 1-pentanol, followed by addition of 0.28 ml of aqueous AgNP solution at desired volume fractions ( $\phi_{\text{AgNP}}=1.5\%$ , 3% and 6%) and 0.1 ml of 0.18 M sodium citrate to form emulsions. Then, 1 ml of absolute ethanol and 0.18 ml of ammonia solution were added and mixed by shaking. 0.1 ml of TEOS was added to start hydrolysis and condensation reaction for directional growth of silica to synthesize Ag-silica Janus rods. The mixture was left undisturbed overnight to react. In comparison to the synthesis of bare silica rods<sup>21</sup>, AgNPs were suspended inside the water before emulsification. A similar strategy has been applied to synthesize  $\text{Fe}_3\text{O}_4$ -silica<sup>23, 24</sup> and  $\text{MnO}_2$ -silica<sup>22</sup> Janus rods from an aqueous suspension of  $\text{Fe}_3\text{O}_4$  nanoparticles and a solution of manganese sulphate, respectively. In the first case,  $\text{Fe}_3\text{O}_4$  nanoparticles were encapsulated inside the droplets after emulsification while in the second case  $\text{MnO}_2$  nanoparticles were precipitated in situ with the emulsion droplets serving as the reaction vessels. In both cases, the synthesized rods are relatively monodisperse with a particle size similar to that of bare silica rods,

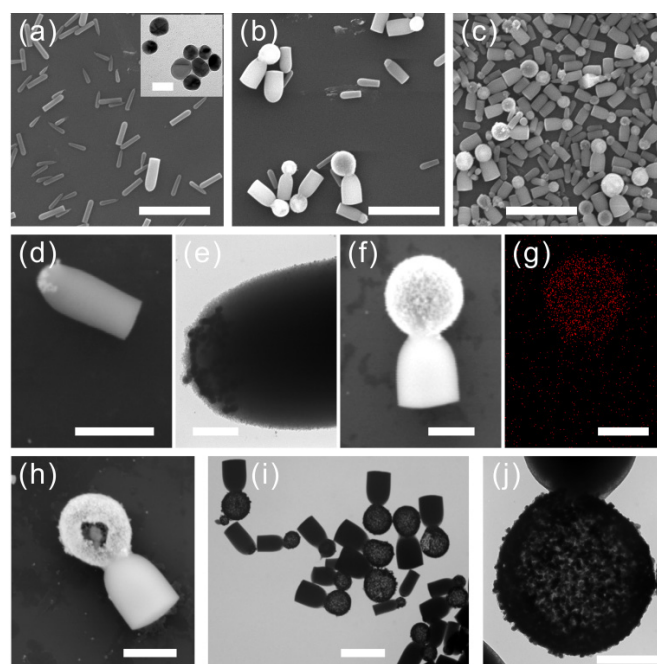


**Figure 1 Characterization of silver-silica colloidal rods.** SEM images of rods synthesized at  $\phi_{\text{AgNP}}$  of (a) 1.5%, (b) 3% and (c) 6%; Inset in (a) is a TEM image of the AgNPs; (d) SEM and (e) TEM images of a particle with a hemispherical end; (f) SEM image and (g) silver element map of a particle with a spherical head; (h) SEM image of a particle with a broken head; (i) TEM image of particles at  $\phi_{\text{AgNP}}=6\%$ , with the head of a typical particle highlighted in (j). Scalebars are 5  $\mu\text{m}$  in (a)-(c), 1  $\mu\text{m}$  in (d), (f)-(h), 2  $\mu\text{m}$  in (i), 200 nm in (j), and 50 nm in the inset of (a).

which suggests that the emulsion droplets are primarily stabilized by PVP and sodium citrate as proposed in the original synthesis<sup>21</sup>. After the reaction was finished, rods were harvested by centrifugation of the solution. The sediment was washed repeatedly by ethanol (3 times) and water (3 times) before it was suspended in water.

### Characterization

Scanning electron microscopy (SEM) was performed either with a Joel JSM-6010LV microscopy at 15 kV or a FEI Quanta 250 FEG microscope at 10 kV. The energy dissipative spectroscopy (EDS) or the element mapping was conducted on the second microscope. Transmission electron microscopy (TEM) was performed on a Hitachi HT-7700 microscope operated at 100 kV. The  $\zeta$ -potential of the Janus rods synthesized at  $\phi_{\text{AgNP}}=6\%$  is determined to be  $-49 \pm 1 \text{ mV}$  using a Brookhaven zeta-potential analyzer (NanoBrook 90Plus PALS).

### Video microscopy

A custom sample chamber was first built by gluing a teflon cylinder (internal dimension: 1 cm; outer dimension: 2 cm; height: 1 cm) onto a piece of coverslip. The chamber was cleaned by isopropyl alcohol and water, dried with nitrogen gas, and treated by oxygen plasma for 1 minute before it was fixed on a microscope stage.

Then, 0.39 ml of  $\text{H}_2\text{O}_2$  solution of desired concentration was loaded, followed by addition of 10  $\mu\text{l}$  of a dilute solution of Janus rods close to the coverslip. The top of the sample chamber was covered by a piece of coverslip to mitigate evaporation. The system was allowed to rest 30 seconds on the stage. All experiments were conducted at room temperature on an inverted light microscope (Olympus IX73) equipped with a 60 $\times$  oil-immersion objective lens (PLAPON; NA=1.42) and a xiQ digital camera (Ximea). Bright field images at the field of view of  $187 \times 187 \mu\text{m}^2$  ( $2048 \times 2048 \text{ pixel}^2$ ) were acquired at 5 frames per second. The motion of the particles was tracked via a standard Matlab script<sup>30</sup>, see Movie S1.

### 3. Results & discussion

The AgNPs are of spherical shape (see the inset of Fig. 1a), with the diameter determined to be  $39 \pm 6 \text{ nm}$  from 80 particles by TEM. Janus rods were synthesized at controlled concentrations of the AgNPs to understand their influence on the rod growth. The resulting particles were characterized through SEM and TEM, see Fig. 1. At low concentration,  $\phi_{\text{AgNP}}=1.5\%$ , the presence of AgNPs has little impact on the rod growth, see Fig. 1a. The resulting particles are of bullet-shape with a hemispherical end and the diameter is approximately 300 nm, similar to rods synthesized when no AgNPs were added<sup>21</sup>. At intermediate concentration,  $\phi_{\text{AgNP}}=3\%$ , large rods of approximately 1  $\mu\text{m}$  with a spherical head emerge besides small bullet-shaped rods, see Fig. 1b. At even higher concentration,  $\phi_{\text{AgNP}}=6\%$ , the majority of the particles are large rods with a spherical head, see Fig. 1c. Smaller particles with a hemispherical head at  $\phi_{\text{AgNP}}=3\%$  are examined more closely in Fig. 1d-e by SEM and TEM, respectively, which reveal that the head is partially covered by AgNPs. Larger particles with a spherical head synthesized at  $\phi_{\text{AgNP}}=6\%$  are examined by a combination of SEM, EDS and TEM, see Fig. 1f-j. In this case, the head is fully covered with AgNPs and the selective localization of AgNPs is confirmed by the silver element mapping, see Fig. 1f-g. Furthermore, we find that the spherical head is hollow, evidenced by a broken end of a particle, see Fig. 1h. This is further confirmed by TEM (see Fig. 1i-j): electrons can more easily pass through the spherical heads, but less so through the silica tails.

The morphology dependence of the resulting particles on the concentration of AgNPs may be explained by the following proposed mechanism, see Fig. 2. First, AgNPs favourably reside at the water-pentanol interface when aqueous AgNP solution is mixed with pentanol to form emulsions, see Fig. 2a. Fig. 1a-c suggests that there are two competing mechanisms at work, which are shown in Fig. 2a. At low concentration, AgNPs only partially cover the water droplets, whose stabilization primarily relies on PVP and sodium citrate. In this case, the droplet size is relatively monodisperse and small (200–300 nm in diameter)<sup>21</sup>. At high concentration, the droplets are fully covered and stabilized by the AgNPs due to the Pickering effect. In this case, the resulting droplets are polydisperse and much larger ( $\sim 1 \mu\text{m}$  in diameter). At intermediate concentration, both stabilization mechanisms take place and the relative occurrence is tuned by the concentration of AgNPs. For both cases, the AgNPs act as the nucleation sites for the initial precipitation of silica. For partially covered droplets, AgNPs appear

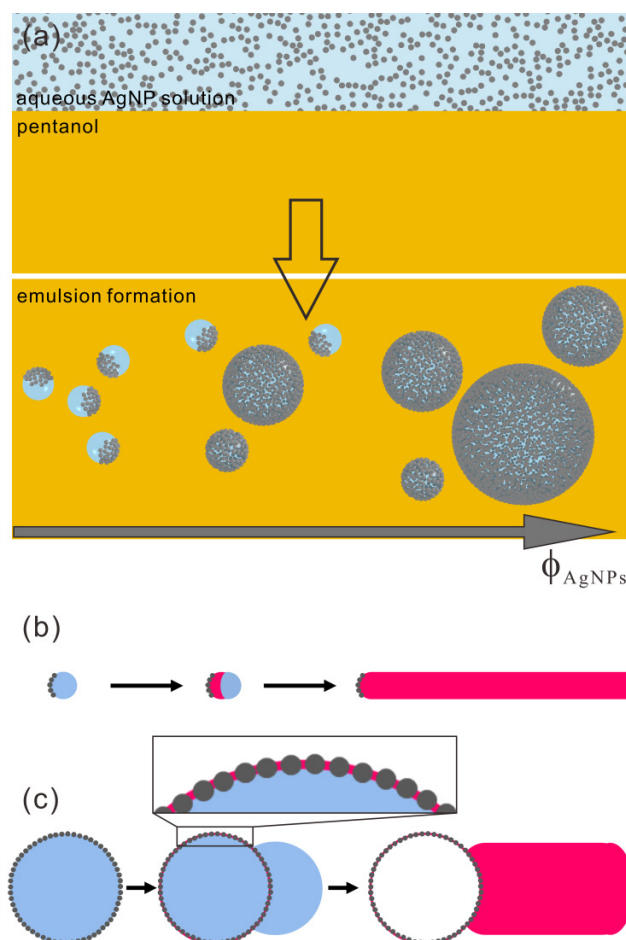


**Figure 2** Schematics on the mechanism of silver-silica rod growth.

(a) An aqueous suspension of AgNPs was mixed with pvp/pentanol and sodium citrate to form an emulsion, with the droplets stabilized by PVP and sodium citrate (partially covered ones) or by AgNPs (fully covered ones), tuned via the concentration of the AgNPs. (b) For droplets stabilized by PVP and sodium citrate, the resulting rods are in general thin. (c) For droplets stabilized by the AgNPs, silica (shown in red) first precipitates at where the nanoparticles reside and form a solid silica shell; meanwhile, water is partially pushed out, followed by directional growth of silica, which results in rods with a much larger diameter.

to form aggregates at the interface, which might be due to the van der Waals attraction<sup>31</sup>. As more silica is precipitated, water will be pushed to the end that is opposite to the AgNPs, see Fig. 2b, which results in subsequent directional growth of silica due to the asymmetric supply of chemicals<sup>21</sup>. For fully covered droplets, the nucleation of silica at the AgNPs leads to the formation of a thin silica shell first and meanwhile water is partially pushed out, see Fig. 2c. The solid shell will prevent or slow down further precipitation of silica inside, while the water droplet outside will lead to directional silica growth, similar as shown in Fig. 2b. In both cases, the water droplet size seems to be the determining factor for the diameter of the rods synthesized, as shown previously<sup>21, 22</sup> and evidenced by the similar diameter of the head and the tail of the particles. Note that the mechanism here for synthesizing Ag-silica particles is different from those for synthesizing  $\text{MnO}_2$ -silica<sup>22</sup> and  $\text{Fe}_3\text{O}_4$ -silica<sup>23, 24</sup>

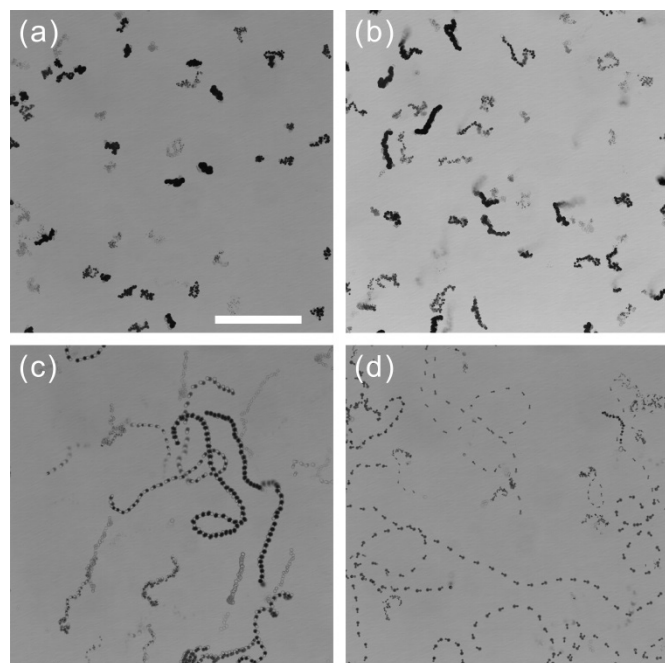
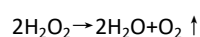


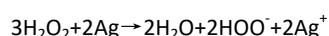
**Figure 3 Self-propelled motion of silver/silica motors.** Minimum projection of 50 images with a time interval of  $\Delta t=0.4$  s at  $\text{H}_2\text{O}_2$  concentrations of (a) 0, (b) 0.001, (c) 0.03 and (d) 0.1w%. The scalebar is 50  $\mu\text{m}$ .

particles and yield particles with a hollow active head and a much larger diameter.

The Janus architecture of the synthesized particles will facilitate active motion due to the high activity of silver with  $\text{H}_2\text{O}_2$ . Silver can trigger two chemical reactions: catalyzing the decomposition of  $\text{H}_2\text{O}_2$  into water and oxygen<sup>32</sup>,



and reacting with  $\text{H}_2\text{O}_2$  and releasing  $\text{Ag}^+$  and  $\text{HOO}^-$  ions<sup>33</sup>,



Since AgNPs are site-selectively located at the head of the rods, we expect that the symmetry of chemical reactions will be broken around the particles, leading to asymmetric release of  $\text{O}_2$ , and  $\text{Ag}^+$  and  $\text{HOO}^-$  ions. As a result, the particles display self-propelled dynamics in the presence of  $\text{H}_2\text{O}_2$ .

We find that particles with a spherical head are much more motile than those with a hemispherical head. Therefore, we only focus on the dynamics of Janus rods synthesized at high concentration of AgNPs,  $\phi_{\text{AgNP}}=6\%$ , since most of the synthesized particles have a spherical head. The concentration of  $\text{H}_2\text{O}_2$  was varied to study its effect on the self-propelled motion. We first examine the dynamics by projecting a time-series of images onto a single image, see Fig. 3. With increasing  $\text{H}_2\text{O}_2$  concentration, the particle trajectories become more extended. At a fuel concentration of 0.1w%, the particles already can move a few times of its body length in 0.4-second intervals. Furthermore, we find that particles self-propel towards their silver-enriched end.

Tempting mechanisms to account for the self-propelled motion are bubble propulsion<sup>16</sup>, self-diffusiophoresis based on neutral solutes<sup>12</sup> and electrolytes<sup>27</sup>. The first two mechanisms can be ruled

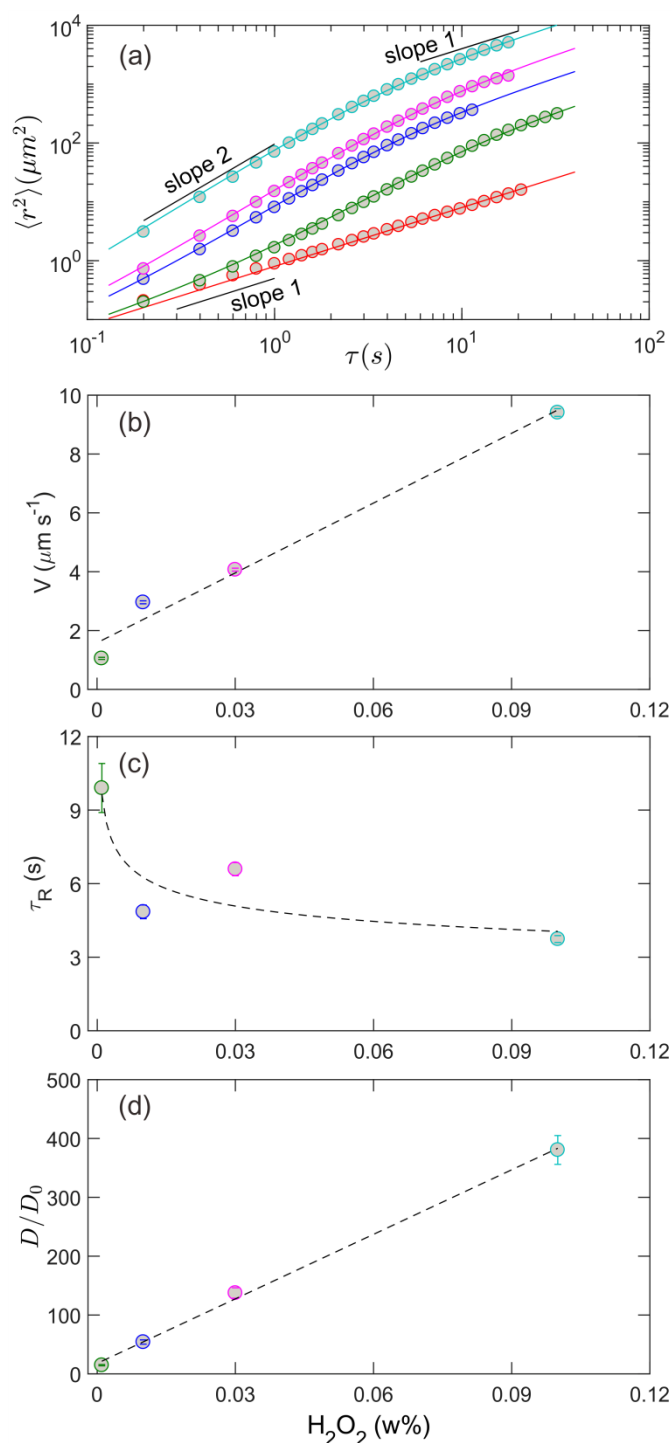


**Figure 4 Motion characterizations.** (a) MSDs of particles at controlled  $\text{H}_2\text{O}_2$  concentrations of 0, 0.001, 0.003, 0.03 and 0.1w% from bottom to top. Solid lines are fits to eq.1. (b) and (c) are the propulsion speed and rotational relaxation time extracted from the fits, respectively. (d) Enhanced diffusivities at long time. Dashed lines in b-d are a guide to the eyes.

out immediately since they predict the opposite direction of propulsion. On the other hand, electrolyte-based diffusiophoresis<sup>27</sup> relies on an electric field set up by the concentration gradient of cations and anions that diffuse at different rates, which drives a charged particle move. This presumably is the mechanism that



leads our particles self-propel, see Fig. S1. First, silver reacts with  $\text{H}_2\text{O}_2$  and the broken symmetry of our Janus particles will result in a higher concentration of released ions,  $\text{Ag}^+$  and  $\text{OOH}^-$ , near the silver end. Furthermore, the cation  $\text{Ag}^+$  has been determined to diffuse at a rate of  $1.65 \times 10^{-9} \text{ m}^2/\text{s}$ , which is much faster than that of the anion  $\text{OOH}^-$ , which is  $0.3 \times 10^{-9} \text{ m}^2/\text{s}$ <sup>25</sup>. As a result, a local electric field pointing to the silver end is generated. Finally, the average zeta-potential of our particles is measured to be  $-49 \pm 1 \text{ mV}$ . The electric field will drive the negatively charged particles move towards the silver head, which is in agreement with our observation.

To quantitatively characterize the motile dynamics, we track the motion of particles via a standard Matlab script<sup>30</sup>. We calculate the mean squared displacements (MSDs) and present the results in Fig. 4a. Without  $\text{H}_2\text{O}_2$ , the particles display Brownian (diffusive) motion. With the presence of  $\text{H}_2\text{O}_2$ , the system in addition displays self-propelled motion. The self-propelled motion competes with random Brownian motion, leading to various dynamic regimes. This is most clearly shown at a low fuel concentration of 0.001w%. At the shortest time scale ( $< 0.4 \text{ s}$ ), the dynamics of the system approaches to that of the Brownian motion, since the accumulated self-propelled motion has not become significant. Yet, as time increases, the accumulated displacement due to directional self-propelled motion becomes increasingly important in comparison to the random Brownian motion, resulting in a superdiffusive regime, followed by a ballistic regime. At even longer time, rotational diffusion of the particles randomizes the orientation of self-propulsion, which leads to enhanced diffusive motion. At higher fuel concentrations, the self-propelled motion already dominates at the shortest time scale we probed, so only the ballistic and enhanced diffusive dynamic regimes are observed.

The MSDs of the particles can be well captured by a persistent random walk model proposed by Howse et al<sup>12</sup>, see Fig. 4a, which is given by equation 1:

$$\langle \Delta r^2 \rangle = 4D_0\tau + \frac{V^2\tau_R^2}{2} \left( \frac{2\tau}{\tau_R} + e^{-2\tau/\tau_R} - 1 \right). \quad (1)$$

In Eq.1,  $\langle \Delta r^2 \rangle$  is the mean squared displacement,  $t$  is the lag time,  $D_0$  is the diffusion coefficient without activity,  $V$  is the self-propelled speed, and  $\tau_R$  is the rotational relaxation time. We first determine  $D_0$  to be  $0.20 \pm 0.05 \mu\text{m}^2/\text{s}$  from the MSD of the control experiment, which contains no hydrogen peroxide. In the presence of hydrogen peroxide, we fit the MSDs to Eq.1 while keeping  $D_0$  fixed to that of the control experiment, assuming that the small amount of hydrogen peroxide does not alter the viscosity of the solvent. From the fits, we can extract the self-propelled velocity ( $V$ ) and the rotational relaxation time ( $\tau_R$ ), see Fig. 4b,c. The self-propelled velocity shows a strong dependence on the fuel concentration, which increases from  $1.06 \pm 0.04 \mu\text{m/s}$  at 0.001w% of hydrogen peroxide to  $9.4 \pm 0.1 \mu\text{m/s}$  at 0.1w% of hydrogen peroxide. It also appears that the rotational diffusion increases i.e. the rotational relaxation time decreases with increasing fuel concentration, but this shows a weaker dependence, see Fig. 4c. At long time, self-propulsion leads to an enhanced

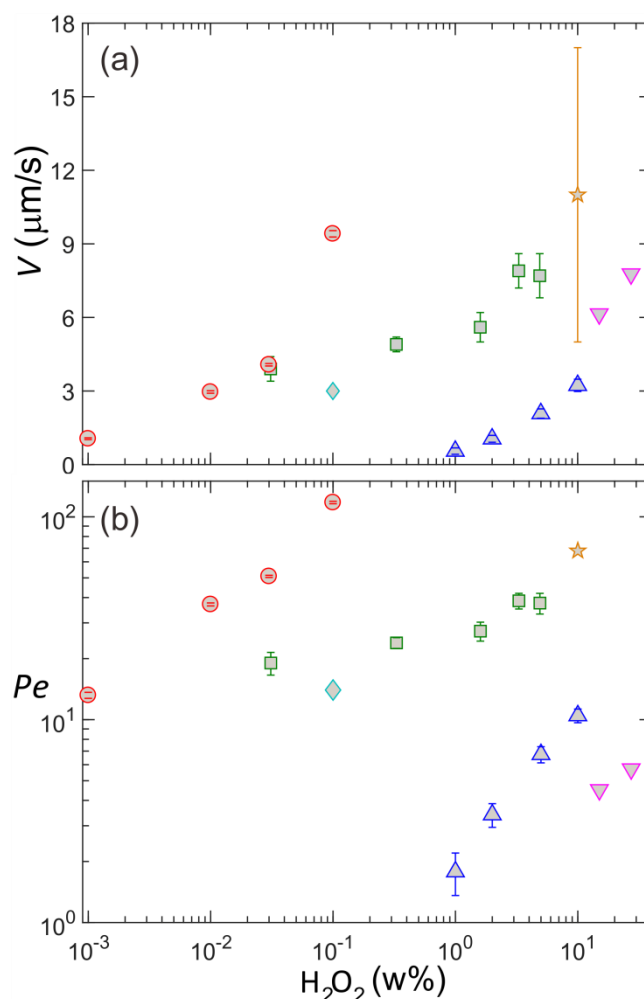


**Figure 5. Comparison of self-propulsion performance.** (a) Self-propelled velocity and (b) corresponding Peclet number as a function of the fuel concentration. The results are shown for our Ag-SiO<sub>2</sub> rods (red circles), and several other representative Pt-based micro/nanomotors, including Au-Pt nanorods (green squares)<sup>11</sup>, Pt coated polystyrene (blue upright triangles<sup>12</sup> and the orange star<sup>13</sup>), silica<sup>14</sup> (purple downward triangles) and gold<sup>15</sup> spheres.

diffusion coefficient of  $D = D_0 + \frac{1}{4}V^2\tau_R$ , which is shown in Fig. 4d for various fuel concentrations. Even at the lowest fuel concentration, 0.001w%, the effective diffusivity is still up to  $15D_0$ . Note that this fuel concentration is comparable to the concentration of  $\text{H}_2\text{O}_2$  detected in the human body<sup>34</sup>. Operating at such low concentration of fuels might be essential for biomedical applications of  $\text{H}_2\text{O}_2$ -based micro/nanomotors. The effective diffusivity increases rapidly to nearly  $400D_0$  at a fuel concentration of 0.1w%.

We further compare the self-propulsion performance of our particles to other well-studied Pt-based micro/nanomotors, including Au-Pt bimetallic rods<sup>11</sup>, Pt-polystyrene<sup>12, 13</sup>, Pt-silica<sup>14</sup>, and Pt-Au spheres<sup>15</sup>. We first compare the self-propelled velocity ( $V$ ) as a function of the fuel concentration, see Fig. 5a. It is clear that our Ag-silica rods display similar self-propelled velocity as other micro/nanomotors, but operating at much lower fuel concentrations. We also use another metrics, the

Peclet number ( $Pe$ ), which is defined as  $Pe = VL/D_0$  and reflects the relative importance of the self-propelled motion to the Brownian motion. Here  $V$  is the self-propelled velocity,  $L$  is the characteristic size of the micro/nanomotors, and  $D_0$  is the diffusion coefficient without activity. We present the results in Fig. 5b. Our micromotors clearly display better performance, i.e. operating at much lower fuel concentrations or higher efficiency, compared to existing Pt-based micro/nanomotors. Even comparing to the to-date most motile Pt-based micro/nanomotors, our particles still reduce the fuel concentration by two orders of magnitude while maintaining the same  $Pe$ .

Several factors may have contributed to the high performance of our particles. Firstly, our particles self-propel via electrolyte-based diffusiophoresis which generally produces faster transportation than neutral self-diffusiophoresis<sup>19</sup> employed by most other studies. Secondly, the large, rough and hollow head provides a large active surface area, which promotes reaction of silver with hydrogen peroxide and thus enhances self-propelled motion<sup>35</sup>. Lastly, rodlike shape might also be beneficial for swimming in a fluid environment when comparing to spheres, e.g. it extends the time for rotational randomization and therewith the time for directional motion.

Interestingly, adding Ag to the Au segment of Au-Pt nanorods has been shown to be an effective means to tune the speed of self-propulsion<sup>36</sup>, which first increases with the content of silver and then decreases as the segment approaches to pure silver. The improvement of self-propelled performance is ascribed to a high rate of hydrogen peroxide decomposition at the Ag/Au alloys and an increase in the mixed potential difference of the two segments, both of which positively influence the self-propelled speed of the nanorods<sup>11</sup>. Furthermore, the presence of  $Ag^+$  in  $H_2O_2$  solution has also led to improved performance of Au-Pt nanorods<sup>3,37</sup>. It was shown that silver ions were reduced into silver on the surface of nanorods. Three possible mechanisms were proposed to account for the behaviour, including the above mentioned one (high rate of decomposition and an increase in the mixed potential difference), improved catalytic activity in the Pt segment and electrolyte self-diffusiophoresis. Since both Au and Pt are absent in our particles and the self-propulsion performance shows a nonmonotonic dependence on the silver content, we rule out the first two mechanisms. We therefore believe that electrolyte self-diffusiophoresis plays a key role, in combination with the relatively large surface area and the slender shape of our particles.

## 4. Conclusions

We have developed a simple Pickering-emulsion based method that can produce silver-silica micro-rods in bulk quantity. We show that these micro-rods carry negative surface charges and self-propel towards their active ends by reacting with hydrogen peroxide, which is consistent with active motion caused by an electrolyte-based self-diffusiophoresis. The self-propelled motion is tuneable

by the fuel concentration, which competes with the Brownian motion, leading to dynamics that can be modelled as a persistent random walk. Furthermore, our micromotors operate at very low fuel concentrations, at a reduced fuel concentration by two orders of magnitude, when compared to the most efficient Pt-based micro/nanomotors. We expect our colloids to enable new applications for micro/nanomotors, especially when large quantities, reduced cost and low fuel concentrations are required<sup>20</sup>.

## Conflicts of interest

There are no conflicts to declare.

## Acknowledgements

Y.G. acknowledges financial support from the General Program of National Natural Science Foundation of China (Project no. 11774237) and the Science and Technology Innovation Commission of Shenzhen (JCYJ20170818141727254).

## References

- 1 S. Sanchez, L. Soler and J. Katuri, *Angew. Chem.*, 2015, **54**, 1414-1444.
- 2 J. Wang, *Lab Chip*, 2012, **12**, 1944-1950.
- 3 D. Patra, S. Sengupta, W. Duan, H. Zhang, R. Pavlick and A. Sen, *Nanoscale*, 2013, **5**, 1273-1283.
- 4 L. Soler, V. Magdanz, V. M. Fomin, S. Sanchez and O. G. Schmidt, *ACS Nano*, 2013, **7**, 9611-9620.
- 5 M. C. Marchetti, J. F. Joanny, S. Ramaswamy, T. B. Liverpool, J. Prost, M. Rao and R. A. Simha, *Rev. Mod. Phys.*, 2013, **85**, 1143-1189.
- 6 G. Popkin, *Nature*, 2016, **529**, 16-18.
- 7 J. Elgeti, R. G. Winkler and G. Gompper, *Rep. Prog. Phys.*, 2015, **78**, 056601.
- 8 E. M. Purcell, *Am. J. Phys.*, 1977, **45**, 3.
- 9 R. Golestanian, T. B. Liverpool and A. Ajdari, *Phys. Rev. Lett.*, 2005, **94**, 220801.
- 10 R. Golestanian, T. B. Liverpool and A. Ajdari, *New J. Phys.*, 2007, **9**, 126-126.
- 11 W. F. Paxton, K. C. Kistler, C. C. Olmeda, A. Sen, S. K. St Angelo, Y. Cao, T. E. Mallouk, P. E. Lammert and V. H. Crespi, *J. Am. Chem. Soc.*, 2004, **126**, 13424-13431.
- 12 J. R. Howse, R. A. Jones, A. J. Ryan, T. Gough, R. Vafabakhsh and R. Golestanian, *Phys. Rev. Lett.*, 2007, **99**, 048102.
- 13 A. Brown and W. Poon, *Soft Matter*, 2014, **10**, 4016-4027.
- 14 H. Ke, S. Ye, R. L. Carroll and K. Showalter, *J. Phys. Chem. A*, 2010, **114**, 5462-5467.
- 15 I. Theurkauff, C. Cottin-Bizonne, J. Palacci, C. Ybert and L. Bocquet, *Phys. Rev. Lett.*, 2012, **108**, 268303.
- 16 J. G. Gibbs and Y. P. Zhao, *Appl. Phys. Lett.*, 2009, **94**, 163104.
- 17 J. L. Anderson, *Annu. Rev. Fluid Mech.*, 1989, **21**, 61-99.
- 18 W. F. Paxton, S. Sundararajan, T. E. Mallouk and A. Sen, *Angew. Chem.*, 2006, **45**, 5420-5429.

- 19 D. Velegol, A. Garg, R. Guha, A. Kar and M. Kumar, *Soft Matter*, 2016, **12**, 4686-4703.
- 20 H. Wang and M. Pumera, *Chem. Rev.*, 2015, **115**, 8704-8735.
- 21 A. Kuijk, A. van Blaaderen and A. Imhof, *J. Am. Chem. Soc.*, 2011, **133**, 2346-2349.
- 22 A. R. Morgan, A. B. Dawson, H. S. McKenzie, T. S. Skelton, R. Beanland, H. P. W. Franks and S. A. F. Bon, *Mater. Horiz.*, 2014, **1**, 65-68.
- 23 Y. Gao, A. K. Balin, R. P. Dullens, J. M. Yeomans and D. G. A. L. Aarts, *Phys. Rev. Lett.*, 2015, **115**, 248301.
- 24 Y. Gao, F. Romano, R. P. A. Dullens, J. K. Doye and D. G. A. L. Aarts, *Phys. Rev. Mater.*, 2018, **2**, 015601.
- 25 N. Chaturvedi, Y. Hong, A. Sen and D. Velegol, *Langmuir*, 2010, **26**, 6308-6313.
- 26 A. Sen, M. Ibele, Y. Hong and D. Velegol, *Faraday Discuss.*, 2009, **143**, 15-27.
- 27 Y. Hong, D. Velegol, N. Chaturvedi and A. Sen, *Phys. Chem. Chem. Phys.*, 2010, **12**, 1423-1435.
- 28 W. Z. Teo, H. Wang and M. Pumera, *Chem. Comm.*, 2016, **52**, 4333-4336.
- 29 I. Washio, Y. Xiong, Y. Yin and Y. Xia, *Adv. Mater.*, 2006, **18**, 1745-1749.
- 30 Y. Gao and M. L. Kilfoil, *Opt. Express*, 2009, **17**, 4685-4704.
- 31 F. Bresme and M. Oettel, *J. Phys.: Condens. Matter*, 2007, **19**, 413101.
- 32 F. T. Maggs and D. Sutton, *Trans. Faraday Soc.*, 1958, **54**, 1861-1870.
- 33 T. R. Kline and A. Sen, *Langmuir*, 2006, **22**, 7124-7127.
- 34 B. Halliwell, M. V. Clement and L. H. Long, *FEBS letters*, 2000, **486**, 10-13.
- 35 N. S. Zacharia, Z. S. Sadeq and G. A. Ozin, *Chem. Commun.*, 2009, **0**, 5856-5858.
- 36 U. K. Demirok, R. Laocharoensuk, K. M. Manesh and J. Wang, *Angew. Chem.*, 2008, **47**, 9349-9351.
- 37 D. Kagan, P. Calvo-Marzal, S. Balasubramanian, S. Sattayasamitsathit, K. M. Manesh, G. U. Flechsig and J. Wang, *J. Am. Chem. Soc.*, 2009, **131**, 12082-12083.